A *Chlamydia* effector recruits CEP170 to reprogram host microtubule organization

Maud Dumoux[1], Anais Menny[1] [†], Delphine Delacour[2], Richard D. Hayward[1*]

[1]Institute of Structural and Molecular Biology, Birkbeck and University College London, Malet Street, London, WC1E 7HX, UK.

[2]Cell Adhesion and Mechanics Group, Institut Jacques Monod, CNRS UMR7592, Université Paris Diderot, 15 rue Helene Brion, 75013 Paris, France.

[†]current address: Institut Pasteur, Channel Receptor Unit, 25 rue du Dr Roux, 75015 Paris, France.

*corresponding author email : richard.hayward@ucl.ac.uk tel : +44 (0)207 631 6553

Abstract:

The obligate intracellular bacterial pathogen *Chlamydia trachomatis* deploys virulence effectors to subvert host cell functions enabling its replication within a specialized membrane-bound compartment termed an inclusion. The control of the host cytoskeleton is critical for *Chlamydia* uptake, inclusion biogenesis and cell exit. Here we demonstrate how a *Chlamydia* effector rearranges the microtubule network by initiating organization of the microtubules at the inclusion surface. We identified an inclusion-localized effector sufficient to interfere with microtubule assembly that we term inclusion protein acting on microtubules (IPAM). We established that IPAM recruits and stimulates the centrosomal protein 170kDa (CEP170) to hijack the microtubule organizing functions of the host cell. We show that CEP170 is essential for chlamydial control of host microtubule assembly, and is required for inclusion morphogenesis and bacterial infectivity. Together, we demonstrate how a pathogen effector reprograms the host microtubule network to support its intracellular development.

Introduction:

Chlamydiae are obligate intracellular pathogens that remain the leading bacterial cause of sexually transmitted disease worldwide and blinding trachoma in developing nations. Increasing evidence also suggests that chlamydial infection may contribute to tumorigenic processes in cervical cancer (Smith et al., 2004; Koskela et al., 2000).

Adherent chlamydial elementary bodies (EBs) employ a type III secretion system (T3SS) to deliver effectors that induce the reorganization of the actin cytoskeleton, promoting membrane deformation that triggers EB uptake into target cells. After internalization, individual EBs are encapsulated within vacuoles derived from the host plasma membrane. These vacuoles are rapidly diverted from the endocytic pathway and instead traffic to the perinuclear region, where they coalesce to form a larger specialized compartment termed the inclusion. In this environment, the bacteria differentiate into reticulate bodies (RBs) and actively replicate (Abdelrahman and Belland, 2005).

A family of hydrophobic T3SS effectors called inclusion proteins (Incs) localize to the boundary membrane of the inclusion. Incs are key mediators of *Chlamydia*-host interactions together with other effectors that are delivered into the host cytosol and nucleus (Peters et al., 2007). Although most effector activities remain uncharacterized, inclusion biogenesis and bacterial growth are dependent upon the recruitment of Golgi-derived vesicles (Carabeo et al., 2003), multivesicular bodies (Beatty, 2006), lipid droplets (Cocchiaro et al., 2008) and the rough endoplasmic reticulum (Dumoux et al., 2012).

In addition to hijacking host organelles, *Chlamydia* also exploits the cytoskeleton to support its lifecycle. For instance, the T3SS effector Tarp is translocated during entry and promotes actin polymerization beneath the plasma membrane both directly and indirectly by stimulating the Arp2/3 complex (Jewett et al., 2006; Lane et al., 2008). An actin and intermediate filament cage is required for the integrity of mature inclusions (Kumar and Valdivia, 2008), and an acto-myosin-dependent process regulates inclusion extrusion from the infected cell (Hybiske and Stephens, 2007). Early *Chlamydia*-containing vacuoles utilize microtubules (MTs) to migrate from the cell periphery towards the MT-organizing centre (MTOC) (Richards et al., 2013). Src family kinases regulate the tight association of the nascent and later mature *C.trachomatis* inclusion with the centrosome (Richards et al., 2013; Mital et al., 2010; Grieshaber et al., 2006), and disruption of this interaction forces the bacteria to enter into persistence (Romano et al., 2013; Leonhardt et al., 2007). Additionally, *C.trachomatis* induces centrosome supernumeracy by disrupting the centrosome duplication pathway (Johnson et al., 2009). MTs are also recruited in the vicinity of the chlamydial inclusion (Al-Younes et al., 2011), and MT-dependent transport processes sequester secretory traffic into the mature inclusion (Carabeo et al., 2003). However, how microtubule organization is initiated and controlled by *C.trachomatis* remains unknown. We hypothesized that a chlamydial Inc protein might be important to initialize MT organization at the inclusion surface.

Here, we identified IPAM as an inclusion protein acting on MT. We demonstrated that ectopic expression of the predicted cytosol-exposed C-terminal domain of this Inc (IPAM-CTD) is sufficient to disturb the MT organizing activity of the cell. We used purified full-length IPAM in pull-down assays and identified the centrosomal protein

170kDa (CEP170) as a host target by mass spectrometry. IPAM-CTD was also sufficient for CEP170 interaction. Next, we demonstrated that CEP170 is a key factor for chlamydial control of MT assembly, a role not ascribed to this protein in non-infected resting cells. CEP170 additionally influences inclusion morphogenesis, host cell shape and chlamydial infectivity. We show that endogenous IPAM and CEP170 act together to promote MT assembly from the inclusion. Together, our data demonstrate the ability of a virulence effector to manipulate the microtubule network to support intracellular bacterial development.

Results:

IPAM- a *Chlamydia* inclusion protein acting on microtubules

Using confocal microscopy, we initially confirmed the arrangement of the MT network during inclusion maturation in detail in HeLa cells (**Fig 1A**). At 12h, MTs assemble at the inclusion periphery, and filaments partially cover this early structure. By 24 h, MTs have entirely surrounded the inclusion from where some filaments extend and contact the plasma membrane. Later (48-66 h), a dense MT scaffold encircles the inclusion. This scaffold is associated with a 'nest' of MTs that originate at the inclusion and extend towards the plasma membrane. The scaffold and nest MT superstructure was even more evident when human osteosarcoma cells (U2OS) were infected with *C.trachomatis* (**Fig 1B**; Nans et al., 2014). Indeed, these cells have a larger cell volume and consequently a cytoskeleton easier to observe in comparison to HeLa cells. In particular, it was easier to discern at later timepoints (48-66 h) that MT actively accumulated around the inclusion periphery in the cell body rather than being compressed against the plasma membrane during inclusion expansion (compare **Fig 1A and 1B 66h**). The initial MT scaffold present at 24 hpi, formed independently of the previously reported actin filament (F-actin) cage (**Fig 1C, 24h**), although inclusion-associated F-actin and MT structures became partially co-incident at later time points (**Fig 1C, 48h and 66h**). Thus, host MTs are progressively organized at the inclusion surface and assemble into an interlinked scaffold and nest superstructure.

The proximity of MTs and the inclusion suggested that a chlamydial effector located in the inclusion membrane might influence this process. As *Chlamydiae* encode Incs, we investigated whether any of these proteins shared sequence homology with MT-interacting proteins. Homology searches revealed that the predicted cytosol-exposed C-terminal domain (CTD) encompassing residues 90-268 of Inc CT223 shared significant primary sequence similarity with human MT and centrosome-interacting proteins including pericentrin (**Fig S1**). In other Incs, similar interfaces enable host protein binding (Delevoye et al., 2008, Rzomp et al., 2006, Scidmore and Hackstadt, 2001). Provocatively, CT223 localizes to the inclusion membrane during infection (Bannantine et al., 2000), and the expression of CT223-CTD in cultured cells is correlated with cytokinesis defects (Alzhanov et al., 2009), a cellular process in which MT dynamics are key (D'Avino et al., 2005). We hereafter refer to CT223 as <u>i</u>nclusion <u>p</u>rotein <u>a</u>cting on <u>m</u>icrotubules (IPAM).

Consequently, we initially investigated the localization of endogenous IPAM in cells infected with *C.trachomatis*, and any relationship to the host centrosome. We confirmed that IPAM was present at the inclusion membrane (Bannantine et al., 2000), throughout the infection timecourse (**Fig 1D**). Strikingly, IPAM predominantly accumulated in defined patches at the inclusion periphery that frequently coincided with or were closely apposed to the centrosomes (**Fig 1D, 1E** and **Fig S2A**). Centrosome supernumeracy was also evident (**Fig 1D**; Johnson et al., 2009).

Given that endogenous IPAM patches are located at the inclusion periphery in proximity to the centrosome, we next investigated the effects of IPAM on the centrosome and MT organization in the absence of infection. We transiently expressed IPAM$^{90-268}$ as a GFP fusion in cultured cells. GFP-IPAM$^{90-268}$ localized with centrosomal proteins γ-tubulin and pericentrin (representative images in **Fig 2A**), showing that IPAM is sufficient to associate with the centrosome, and therefore with the principal <u>micro</u>tubule <u>o</u>rganizing <u>c</u>enter (MTOC) of the cell. Super-resolution structural illumination microscopy (SIM) revealed that GFP-IPAM$^{90-268}$ is in close apposition to γ-tubulin and pericentrin, rather than co-localized, suggesting IPAM$^{90-268}$ association with the pericentriolar matrix (PCM) and/or MT minus-ends (**Fig 2B**). Moreover, GFP-IPAM$^{90-268}$ expression induced centrosomal abnormalities including supernumeracy of γ-tubulin and pericentrin puncta and even the loss of defined

centrosomes in some cells (**Fig 2C** and **Fig S2B**). The most pronounced effect was on pericentrin distribution (**Fig 2D**). Altogether, these data demonstrate that IPAM$^{90\text{-}268}$ targets and destabilizes the host PCM.

As the main function of the MTOC is to assemble and organize MT, we observed the MT network in cells transfected with IPAM$^{90\text{-}268}$. At low expression levels, GFP-IPAM$^{90\text{-}268}$ is located exclusively at the center of the MT array, which appeared structurally indistinguishable from that in control cells (**Fig 2E**). However, increased GFP-IPAM$^{90\text{-}268}$ expression provoked some MT disorder but did not affect F-actin architecture at steady state (**Fig 2E and Fig S3A**). In dividing cells, GFP-IPAM$^{90\text{-}268}$ localized to the spindle pole and apparently partitioned preferentially to one centriole (**Fig 2F**). This mobility confirmed the strong affinity of GFP-IPAM$^{90\text{-}268}$ for the centrosome, which is retained even during physiological remodeling of the MT, and suggests that ectopically expressed IPAM$^{90\text{-}268}$ is unlikely to be forming inactive cytosolic aggregates.

Given the effect of IPAM$^{90\text{-}268}$ on the PCM and the robust relationship between the pericentriolar material and MT organization (Woodruff et al., 2014), we analyzed the impact of IPAM expression on MT assembly following MT depolymerization and regrowth. GFP-IPAM$^{90\text{-}268}$ localization remained unchanged after MT disassembly (**Fig S3B**), indicating MT-independent association of IPAM$^{90\text{-}268}$ with the centrosome. Moreover, the presence of GFP-IPAM$^{90\text{-}268}$ did not interfere with MT depolymerisation upon induced disassembly (**Fig S3C**). After 5 min regrowth, GFP-IPAM$^{90\text{-}268}$ remained enriched at the centrosome, and additional GFP-IPAM$^{90\text{-}268}$ foci were observed along newly polymerized MTs (**Fig 2G**). Higher levels of expressed GFP-IPAM$^{90\text{-}268}$ generated multiple MT nucleation foci within individual cells (**Fig 2G**). Nucleated MTs were non-homogenous in length and appeared to form a randomly oriented network. When examined at higher resolution by SIM, it was evident that even low-level GFP-IPAM$^{90\text{-}268}$ expression was sufficient to alter nucleation foci and generated shorter and interconnected emergent MT networks in comparison to those in GFP-control cells (**Fig 2H**). Multi-foci MT networks were apparent in 62.9±1.2% of GFP-IPAM$^{90\text{-}268}$ transfectants versus 11.1±1.6% of GFP-control cells (**Fig 2I**). Thus, IPAM-CTD perturbs MT organization and assembly.

Therefore, we demonstrate that IPAM-CTD, which shares homology with eukaryotic

centrosomal and MT-related proteins, targets the main cellular MTOC and destabilizes the PCM. Consequently, the microtubule organizing activity of the MTOC is disturbed, even when IPAM-CTD is expressed at low levels. Furthermore, when IPAM[90-268] is overexpressed, ectopic MT nucleation foci are formed. Together, these data show that IPAM associates with the PCM at the centrosome and is sufficient to hijack the microtubule organizing function of the host cell.

Chlamydia IPAM interacts with host CEP170 to perturb MT assembly

To identify eukaryotic interacting partners using a pull-down approach, we expressed IPAM in *Escherichia coli*. Full-length hydrophobic IPAM partitioned predominantly to the bacterial membrane fraction (**Fig 3**), from where it could only be solubilized with detergent, indicating insertion of IPAM into the *E.coli* membrane. Further purification was carried out under native conditions (**Fig 3**; see *Materials and Methods*). Exploiting the affinity tag, we performed a pull-down assay using purified IPAM and human cell extract (see *Materials and Methods*), and identified twelve candidate interacting proteins by mass spectrometry. Of these, six were MT and centrosome related, the most significant being c̲entrosomal p̲rotein 170 (CEP170; Mascot score 65.56, 2 peptides read 10 times each). CEP170 is a component of the mother centriole that interacts with kinesin-like motors during cell division (Maliga et al., 2013; Welburn and Cheeseman, 2012; Guarguaglini et al., 2005). Furthermore, CEP170 overexpression disturbs centrosomal positioning and the MT network (Guarguaglini et al., 2005). Given the similar effects of IPAM-CTD expression on the centrosome and MTs (**Fig 2**) we focused on examining potential interplay between IPAM and CEP170 during *C.trachomatis* inclusion biogenesis.

GFP-IPAM[90-268] was co-isolated following immunoprecipitation of CEP170 from transfected cells (**Fig 4A**). Reciprocally, endogenous CEP170 was co-purified when GFP-IPAM[90-268] was immunoprecipitated from transfectants (**Fig 4A**). Thus, the IPAM-CTD is sufficient for CEP170 interaction in cells. Immunostaining of endogenous CEP170 in GFP-IPAM[90-268] transfectants demonstrated co-localization of both proteins at the centrosome (**Fig 4B**), consistent with our *in vitro* association data.

Next, we investigated whether CEP170 is required for centrosomal localization of IPAM[90-268]. CEP170 knockdown was confirmed by immunofluorescence and

immunoblotting (**Fig S3D** and **Fig S3E**). Silencing of CEP170, did not release GFP-IPAM$^{90-268}$ from the centrosome, and γ-tubulin and pericentrin localization remained similarly undisturbed (**Fig 4C**), in agreement with previous observations (Guarguaglini et al., 2005). Nevertheless, higher levels of GFP-IPAM$^{90-268}$ expression promoted CEP170 redistribution into additional extra-centrosomal foci, where both proteins co-localized (**Fig 4D** and **E**). While CEP170 is therefore not necessary for the association of GFP-IPAM$^{90-268}$ with the centrosome, GFP-IPAM$^{90-268}$ expression is sufficient to influence CEP170 localization in cells.

Given this dynamic interplay between GFP-IPAM$^{90-268}$ and CEP170, we determined whether CEP170 was required for GFP-IPAM$^{90-268}$-mediated disruption of the centrosome. We examined γ-tubulin and pericentrin in cells expressing control-siRNA or CEP170 siRNA in the presence or absence of GFP-IPAM$^{90-268}$, and classified the resultant centrosomal structures (**Fig S2B**). The nature of the defects particularly in the PCM reported by pericentrin was subtly yet significantly altered when cells received CEP170-siRNA (**Fig 4F** and **4G**), demonstrating a partial role for CEP170 in IPAM-mediated PCM interference. Similarly, we investigated whether CEP170 was necessary for IPAM$^{90-268}$ to disturb MT organization (**Fig 4H**). CEP170 knockdown did not influence the MT organization in GFP-control cells but partially rescues GFP-IPAM$^{90-268}$-induced defects in MT assembly, restoring MT regrowth (**Fig 4H)**. Additionally, the normal MT organization during regrowth in CEP170-siRNA cells (*i.e.* in the absence of GFP-IPAM$^{90-268}$) strongly suggests that CEP170 does not play a housekeeping role in MTOC function *per se*. Consequently, we conclude that the interaction between IPAM$^{90-268}$ and CEP170 is functional.

Taken together, we show that IPAM interacts with the host protein CEP170. While IPAM$^{90-268}$ localization to the centrosome is CEP170-independent, the effect of IPAM$^{90-268}$ on PCM and the MT organization is mainly CEP170-dependent.

CEP170 influences MT organization via IPAM in infected cells

As IPAM is sufficient for CEP170 interaction, we next examined the relative location of endogenous IPAM and CEP170 in cultured HeLa and U2OS cells infected with *C.trachomatis.* CEP170 was present in patches at the inclusion membrane from 24 hpi and multiple patches were evident at 66hpi (**Fig 5**). Consistent with the *in vitro*

interaction and the effects of IPAM$^{90-268}$ in cultured cells, co-localization between IPAM and CEP170 was observed at the inclusion, although as might be expected during infection, both IPAM and CEP170 were additionally present in isolation (**Fig 5**). Since CEP170 influences MT organization only in the presence of IPAM, we investigated the effect of silencing CEP170 expression on MT organization during inclusion biogenesis. CEP170 knockdown remained stable for the duration of the infection cycle (**Fig S3D** and **S3E**), and did not significantly influence the early phase (<24 h) of bacterial development in cultured cells (**Fig S3F**). Although Nigg and co-workers suggested that CEP170 knockdown in HeLa cells induced a change in cell shape from a cobblestone to elongated phenotype (Guarguaglini et al., 2005), under our growth conditions, non-infected HeLa cells remained elongated independently of CEP170 knockdown (**Fig 6A**). Nevertheless, after infection with *C.trachomatis*, simultaneous CEP170 knockdown resulted in rounding of the infected cells whereas infected control-siRNA cells remained elongated at both 48 h and 66 h (**Fig 6A, Fig S2E** and **Fig S4A**). This indicated a significant CEP170-dependent change in host cytoskeletal organization in infected cells. To investigate this, we visualized the MT network in these two cell populations. In the infected control cells, the MT network displayed a radial organization where MTs emerge from the CEP170-positive MTOC to form the characteristic MT scaffold and nest. In equivalently infected CEP170 knockdown cells, there were profound alterations; a partial MT scaffold was formed by an array of parallel MTs without a distinct point of emergence, and the MT nest was absent, driving the distinct rounded cell phenotype (**Fig 6B** and Fig **S4A**). Nevertheless, the extent of co-localization between F-actin and the MT network surrounding the aberrant-shaped inclusion was not significantly affected in infected CEP170-siRNA cells (**Fig S3G**). Intriguingly in non-infected cells, the MT and F-actin networks in CEP170 knockdown cells were indistinguishable from controls at steady state (**Fig S3H**), correlating with the absence of a change in cell shape in these two populations (**Fig 6A**). This strongly suggests that the CEP170-dependent pathway stimulated by *C.trachomatis* to reorganize MTs is silent in resting uninfected cells or unconventional in infected cells.

To probe further how CEP170 functions relate to IPAM, we examined the consequences of GFP-IPAM$^{90-268}$ overexpression in infected cells in the presence and

absence of CEP170. When expressed in infected cells, GFP-IPAM$^{90-268}$ puncta are enriched at the inclusion, with a minor population present at the cell periphery (**Fig 6C**). Moreover, we observed a more prominent MT scaffold associates with a hyper-developed nest, modifying the cell shape in a distinctive manner in cell expressing endogenous levels of CEP170 (**Fig 6C** and **6D**). This exaggerated phenotype due to the presence of high levels of GFP-IPAM$^{90-268}$ in infected cells is indicative of an IPAM-induced overstimulation rather than a dominant negative effect. In CEP170-siRNA cells, GFP-IPAM$^{90-268}$ overexpression partially reverts the defect in the formation of the MT nest (**Fig 6D**), suggesting that GFP-IPAM$^{90-268}$ is able to compensate for loss of CEP170 via a secondary or redundant pathway.

These data reinforce our view that CEP170 function is extended in infected cells, and that this augmentation depends on IPAM$^{90-268}$. Also, while IPAM$^{90-268}$ preferentially acts with CEP170 to organize MTs, as with other bacterial effectors IPAM can also stimulate redundant pathways, possibly *via* additional interacting partners, to reorganize MTs in the absence of CEP170.

CEP170 is essential for MT assembly, inclusion morphology and *Chlamydia* replication.

Given that CEP170 is a key determinant of MT organization during infection, we next examined MT regrowth to assess the dynamics of this mechanism (**Fig 7**). CEP170 knockdown does not significantly influence MT regrowth in non-infected cells (**Fig S3I** and **S2D**). In infected cells, newly polymerized MTs emerged from single or multiple MTOC and encased the inclusion after 5 min. After 20 min, MT accumulation around the inclusion was less pronounced than at steady state but the nest did reform (**Fig 7**). After CEP170 knockdown, MTs emerged from an enlarged structure following 5 min regrowth at 48 h, and at 66 h tubulin dramatically accumulated at one pole of the inclusion under equivalent conditions (**Fig 7**) demonstrating the critical role for CEP170 in MT assembly. After 20 min regrowth, MTs are present as in control cells, but inclusions lost their typical spherical morphology and appear constricted (**Fig 7**). Indeed, inclusion architecture was severely disrupted, as voids, characterized by the absence of bacteria and MTs in the presence of an intact inclusion membrane were evident (**Fig 7 and S4B**). This is

interesting as it was predicted using experiment-based mathematical models that contact between the bacteria and the inclusion membrane controls chlamydial development (Wilson et al. 2006, Hoare et al. 2008). Consequently, we investigated whether CEP170 is required for chlamydial infectivity. Although siRNA-mediated knockdown inherently generates a mixed population of cells expressing varying levels of CEP170, CEP170 knockdown significantly attenuated the infectivity of *C.trachomatis* progeny ($12.3 \times 10^4 \pm 2.7 \times 10^4$ in control-siRNA versus $6.3 \times 10^4 \pm 2.3 \times 10^4$ in CEP170-siRNA).

These data demonstrate a key role for CEP170 in MT assembly at the inclusion periphery allowing the maintenance of inclusion shape and the success of the chlamydial infectious cycle.

The endogenous IPAM-CEP170 interaction is involved in MT assembly in *C.trachomatis* infected cells.

Using transfected cells and knockdown approaches, we demonstrate that the IPAM-CTD perturbs MT assembly via its interaction with CEP170, which is essential for MT organization in infected cells. Next, we investigated the nature of the MT nucleation centers in infected cells, examining endogenous IPAM and CEP170. In order to facilitate the observation of the point of emergence of MTs, we performed a MT regrowth assay for 5 min. At 48 hpi, 75% of infected cells showed multiple points of MT nucleation on the inclusion, which are ubiquitously observed by 66hpi in both HeLa and U2OS cells (**Fig 8A** and **Fig 8B**). Interestingly, these MTOCs are distributed across the 3D volume of the inclusions either individually or as groups (**Fig 8A** and **Fig 8B**, insets showing different z positions).

In both cell lines, ~95% of inclusion-associated MT nucleation foci contained CEP170 in defined points or more diffusely. Occasionally, patches of co-localized IPAM and CEP170 are observed without emerging MTs, although 50% and 60% of the CEP170-positive MT nucleation foci localize with IPAM patches in HeLa and U2OS cells, respectively (**Fig 8A** and **Fig 8B**) indicating the presence of the IPAM-CEP170 complex in at least half of inclusion-associated MT nucleation centers captured by this method in infected cells.

These data reveal that endogenous IPAM and CEP170 cooperate at the surface of the inclusion to orchestrate host MT reorganization.

Discussion:

We demonstrate that *Chlamydia trachomatis* integrates a transmembrane effector, IPAM, into the inclusion membrane to locally hijack host MT organizing activity by recruiting CEP170. We propose that this event leads to the formation of a MT 'scaffold and nest' superstructure necessary to maintain cell and inclusion morphology, which is consequently required for bacterial infectivity. Moreover, we show that CEP170 exhibits additional roles in MT organization when compared to resting cells.

IPAM shares sequence similarity with MT and centrosomal proteins. We confirmed that the *C.trachomatis* inclusion traffics to and associates with the MTOC (Richards et al., 2013; Grieshaber et al., 2006) and demonstrated the proximity of endogenous IPAM patches and the centrosome. When IPAM-CTD is expressed in cells, it localizes to the centrosome, the principal MTOC. IPAM$^{90-268}$ induces centrosomal abnormalities with a pronounced effect on the organization of the PCM. This is intriguing considering that centrosomal dysfunction is correlated to aneuploidy and tumor initiation (Nigg, 2002) and that *C.trachomatis* infection is associated with cervical cancer (Smith et al., 2004; Koskela et al., 2000).

Consequently, the MTOC is able to generate MTs, but their organization is disrupted. When IPAM$^{90-268}$ is overexpressed, multiple MT nucleation centers become evident. These data show that IPAM is sufficient to reprogram the MT organizing activity of the host cell. Intriguingly, in *C.trachomatis* infected cells, multiple MTOC are observed and we demonstrated that 50-60% of the CEP170-positive MT nucleation foci were associated with IPAM.

While IPAM$^{90-268}$ localization to the centrosome is CEP170 independent, IPAM-directed PCM disruption and MT reorganization is largely dependent on CEP170. This demonstrates functional interaction between IPAM$^{90-268}$ and CEP170, and reveals CEP170 activities not previously observed in resting non-infected cells. These extended functions were supported by CEP170 knockdown. In our hands, non-infected cells lacking CEP170 exhibited no detectable abnormalities in cell shape, MT

organization or MT assembly. By contrast, knockdown of CEP170 in *C.trachomatis* infected cells resulted in a reduced MT scaffold and the absence of the MT nest, leading to a characteristic round cell shape. This was accompanied by defects in MT organization during regrowth and changes in inclusion morphology. Thus, CEP170 functions are exacerbated during *C.trachomatis* infection. Indeed, these additional functions highlighted by studying infection could indicate dormant or incompletely understood roles for CEP170 in non-infected non-dividing cells. Intriguingly, overexpression of IPAM[90-268] in infected cells can maintain MT architecture in the absence of CEP170, showing that IPAM can functionally compensate using CEP170-independent secondary or redundant pathways possibly by interacting with additional eukaryotic binding partners.

Our data therefore show that IPAM reorganizes MT indirectly by interacting with CEP170 and possibly other eukaryotic partners. This is distinct from other bacterial effectors including *Chlamydia trachomatis* CopN, which act directly on tubulin subunits to inhibit polymerization (Archuleta et al., 2011). To our knowledge, this is the first example of such significant structural changes in organization of the MT network by an intracellular bacterial pathogen. *Salmonella*, *Brucella* and *Legionella* all exploit the MT network to commandeer vesicular transport, but the associated MT architecture is not profoundly rearranged (Radhakrishman and Splitter, 2012). Only a toxin secreted by the extracellular bacterium *Clostridium* generates localized MT reorganization by inducing MT-derived protrusions (Schwan et al., 2009).

Recently, a population of specialized post-translationally modified MTs was observed surrounding the inclusion, which is required for Rho-dependent tethering of Golgi mini-stacks. It was proposed that *C.trachomatis* must initially reorganize MTs that are subsequently detyrosinated 2 to 3 hours later (Al-Zeer et al., 2014). As the inclusion expands over time, these specialized MTs must be continuously readjusted by a cycle of MT assembly and modification, as also suggested for the actin cage (Kumar and Valdivia, 2008). Our data mechanistically complement and extend this study, as we identify IPAM that initiates MT organization at the inclusion surface by recruiting CEP170. Subsequently, these MTs could be modified by unknown host or additional chlamydial factors, allowing Rho-dependent organelle positioning.

CEP170 binds MT (Guarguaglini et al., 2005), but whether IPAM also engages MT directly or requires CEP170 remains unknown. Moreover, as Incs have the propensity to engage each other in heterotypic Inc-Inc complexes (Gauliard et al. 2015), additional Incs might interact with IPAM at the inclusion membrane and could regulate its activity. For instance, recent evidence suggests that the Inc CT850 binds the MT-associated motor protein dynein (Mital et al. 2015). Moreover, it is known that CEP170 is phosphorylated by Polo-like kinase 1 (Guarguaglini et al., 2005). How the phosphorylation of CEP170 is involved in the formation or activities of the IPAM-CEP170 complex or influence chlamydial infection remains unknown. Further *in vitro* reconstitution experiments are now essential to understand the molecular mechanisms of IPAM- and CEP170-mediated MT and centrosomal subversion in detail, and to delineate the domains of each partner involved in their functional interactions.

Materials and Methods:

Sequence homology searches

The primary amino acid sequences of the 55 predicted inclusion proteins from *C.trachomatis* serovar L2 (Lutter et al., 2012) were compared to the *Homo sapiens* (taxid 9606) database using Blast (blast.ncbi.nlm.nih.gov/Blast.cgi). Results were manually filtered for known MT/centrosomal proteins, and ranked according to the number of identical/similar amino acid residues.

Cell culture, transfection, knock down and infection

HeLa or U2OS cells were routinely cultured in DMEM containing 10% (v/v) fetal calf serum and antibiotics [penicillin (100 Uml^{-1})/streptomycin (100 μgml^{-1}) or gentamicin (25 μgml^{-1}), Invitrogen].

Cells were transfected with pEGFP-C2 or pEGFP-IPAM$^{90-268}$ (300 ngml^{-1}), using Turbofect according to the manufacturer's instructions (Fermentas).

Cells were transfected with 10 nM of siRNA designed against CEP170 sequence or against non-specific sequence, using Hiperfect according to the manufacturer's instructions (Qiagen). Three siRNAs (5'-AAGCATGGAGATTTCTTCTAT-3', 5'-

AAAGTGTTTCTGGAACTTTAA-3', 5'-TTGGATATGATACAAATCTTT-3') directed against CEP170 were independently validated by Western blot and immunofluorescence.

Cells were infected with *C.trachomatis* serovar L2 as previously described (Dumoux et al. 2012).

When these approaches were used in combination, cells (density $4\times10^4\,cm^{-2}$ plated 24 h previously) were transfected with plasmids immediately prior to infection (*i.e.* t=0h), or with siRNA 24 h prior to infection. When appropriate, expression plasmids were transfected 48 h after transfection of siRNA.

Infectivity assay

Bacterial infectivity was tested as previously described (Dumoux et al., 2012).

Microtubule regrowth assay

At an appropriate time point, cells were treated with $10\,ngml^{-1}$ nocodazole (Sigma-Aldrich) for 4 h at 37°C. Steady state cells were directly fixed and stained. "0min" samples were fixed and stained directly after incubation at 4°C for 20 min, whereas 5 min or 20 min samples were appropriately incubated further at 37°C in nocodazole-free media prior to fixation and immunolabelling.

Cell Labeling

For immunolabelling, cells were fixed with either cold methanol (5 min on ice) or 4% (w/v) parafolmaldehyde in cytoskeleton buffer with sucrose (CBS, 10 mM MES, 138 mM KCL, 3 mM MgCl, 2 mM EGTA and 0.32 M sucrose; 30 min, RT), and permeabilized with cold methanol/ethanol or 0.5% (v/v) Triton-X100 in CB. Primary antibodies, anti-IPAM (generous gift from Dan Rockey), anti-CEP170 (Invitrogen), anti-IPAM, anti-α/β-tubulin (Cytoskeleton), anti- β-tubulin (Millipore), anti-γ-tubulin (Abcam) or anti-pericentrin (Covance), were diluted in PBS containing 1% (w/v) bovine serum albumin (BSA) and incubated (3h, RT) prior to incubation with appropriate secondary antibodies (Invitrogen) in the same buffer (1h30, RT). Samples were mounted using Mowiol. 200nM Rhodamine-coupled phalloidin (Invitrogen) was added to the primary antibody mixture. WGA AlexaFluor 594 labeling (45 min, RT) was performed prior to cell permeabilisation. For simultaneous

labeling of IPAM, β-tubulin and CEP170, primary antibodies were appropriately diluted in PBS containing 10% (w/v) BSA and secondary antibodies coupled to AlexaFluor 488, 546 or 633 were selective for mouse IgG subclasses. Controls to exclude cross-reactivity were performed prior to the infection experiments.

Microscopy

Samples were observed using a confocal microscope (TCS Sp5 or Sp8 AOBS; Leica) with an oil-immersion objective (63x, 1.4 NA; Leica) operated in sequential mode. Using the AOBS, emission windows were selected to ensure no leak between channels using equivalent samples labeled with a single fluorophore. Laser reflections were avoided by allowing a distance of at least 10 nm between the laser used for excitation and the start of the corresponding emission window. Optical z-sections were collected every 330nm.

An OMX V3 (API, division of GE Healthcare) was used for super-resolution microscopy. For this technique, coverslips (Zeiss) were mounted using Vectashield instead of Mowiol, and viewed using an oil-immersion objective (100x, 1.4 NA; Olympus). Prior to acquisition, the OTF for each channel were calculated using calibration beads, the color channels aligned, and CCD camera noise corrected. Image acquisition and reconstruction was performed using DeltaVision software.

Image analysis, 3D reconstruction and quantification

All images were analyzed using Fiji (Eliceiri et al., 2012). Greyscale modifications were applied across all conditions, and thresholds remained constant. Maximum intensity projections (max-projection) of a few z-stacks are required to observe the entire MTOC.

The 3D viewer plugin (Schmid et al., 2010) was used for 3D-reconstruction, and the volume displayed as a surface using a constant threshold. Prior to 3D-reconstruction, images were treated using the rolling-ball-background algorithm plugin with a mean filter of 1.5 pixels.

To determine the level of expression, puncta of GFP-IPAM[90-268] were scored from a maximum projection of the entire volume of the cell. Cells with 10 or less puncta were considered as cells expressing low levels of GFP-IPAM[90-268]. For cells expressing

GFP, cells with mean pixel intensity <33% of the maximum grey value were considered as low expressing cells.

When quantification was performed, approximately 150 infected cells and 250 non-infected cells per condition were analyzed. Representative images of the different classifications used are shown in **Fig S2**. Student's t-test was applied for statistical analyses.

Centrosome positioning and IPAM patches **(Fig S2A)***:* a mask of the inclusion was generated as described (Dumoux et al., 2012) without the 'fill hole' option. The inclusion periphery was detected using the 'find edges' option (yellow line) and the outline superimposed back onto the RGB images. Centrosomes (γ-tubulin) in contact with the inclusion periphery were scored manually.

Centrosomal markers (**Fig S2B**): cells (15±7) within fields of view were imaged and max-projection applied to the entire z-stack. After manually tracing cell edges, the number, position and appearance of centrosomal labelling was categorized according to the classification presented in **Fig S2B**.

MT regrowth, low magnification (**Fig S2C**): cells (15±7) within fields of view were imaged and max-projection applied to the entire z-stack. After manually tracing cell edges, the number of MT regrowth foci were quantified according to the criteria presented in **Fig S2C**.

MT regrowth, high magnification (**Fig S2D**): in cases where >97% of the cells exhibited mono-foci according to the criteria presented in **FigS2C**, cells within fields of view (9±3.5) were imaged at higher magnification, and max-projection applied to the entire z-stack. After manually tracing cell edges, MT regrowth foci were assessed manually according to the criteria presented in **Fig S2D**.

Cell shape (**Fig S2E**): cells (15±7) within fields of view were imaged and max-projection applied to the entire z-stack. Confluent cells were excluded. After manually tracing cell edges, the number of round or elongated cells were quantified according to the criteria presented in **Fig S2E**.

Inclusion shape (**Fig S2F**): DNA was stained and cells (9±3.5) within fields of view imaged. Inverted LUT and grey scale modifications were performed uniformly. Manual quantification was performed according to the criteria presented in **Fig S2F.**

Plasmids

pET22b-IPAM was generated by polymerase chain reaction (PCR) amplification of the gene encoding IPAM (CT223) from *Chlamydia trachomatis* serovar L2 genomic DNA. The PCR product, engineered to contain an *Nde*I restriction site at the 5' of the start codon and a *Xho*I restriction site at the 3' end of the gene, was cloned into the corresponding sites of the T7 expression vector pET22b (Novagen) creating an in-frame C-terminal fusion of six histidine residues (expected size: 32kDa).

pEGFP-IPAM$^{90\text{-}268}$ encoding the cytoplasmic domain of IPAM (IPAM$^{90\text{-}268}$) was generated by PCR amplification of the appropriate fragment of the IPAM (CT223) gene from *Chlamydia trachomatis* serovar L2 genomic DNA. The PCR product was engineered to generate an *Eco*RI restriction site followed by a start codon prior to the codon encoding residue 90 of IPAM and a *Kpn*I restriction site at the 3' of the stop codon. This was cloned into the corresponding sites of the expression vector pEGFP-C2 (Clonetech) creating an in-frame N-terminal fusion of green fluorescent protein (GFP) (expected size: 52kDa).

Expression and purification of IPAM

pET22b-IPAM *E.coli* C41(DE3) (Miroux and Walker, 1996) transformants were cultured (200 *g*, 37°C) in Luria's broth (LB) containing ampicillin (50ugml^{-1}) until A$_{600}$~0.8. Protein expression was induced using 0.05 mM isopropyl β-D-thiogalactopyranoside (IPTG, Sigma-Aldrich) and incubation continued (2h, 37°C). Cells were harvested (2000 *g*, 15 min, 4°C) and resuspended in Tris-buffered saline (20 mM Tris HCl pH7.4, 140 mM NaCl; TBS) containing protease inhibitors (Roche), prior to lysis with a pressure cell homogeniser (18000 psi, Stansted). After clarification (2000 *g*, 10 min, 4°C), membranes were separated by centrifugation (31000 *g*, 1h, 4°C). Membranes containing IPAM were incubated with appropriate buffers (TBS, or 20 mM Tris HCl pH7.4, 1 M NaCl; TBS, 100 mM Na$_2$CO$_3$ pH11; 8 M urea) or with 1% (w/v) detergent [ASB-14 (Millipore), Triton X-100 (Sigma-Aldrich), CHAPS (Sigma-Aldrich), dodecyl-β-d-maltoside (Sigma-Aldrich), polyoxyehltylene (Lane et al. 2008) tridecyl ether (Sigma-Aldrich), C7BZ0 (Sigma-Aldrich), octyl-β-d-glucopyrone (Sigma-Aldrich) or octyl-β-d-1-thioglucopyrone (Sigma-Aldrich)] in TBS containing protease inhibitors (Roche). Solubilized material was recovered by

centrifugation (31000 g, 1 h, 4°C). 0.7% (w/v) ASB-14-containing buffer extracted IPAM from the membrane most effectively, and was retained during binding and then elution from nickel nitrilotriacetic acid-agarose, which was carried out under native conditions according to the manufacturer's instructions (Qiagen).

Pull down assay

Purified IPAM was incubated (10 min, RT) with magnetic beads coupled to cobalt (Dynabeads, Invitrogen) before incubation (45 min, rotating, 30 °C) with HeLa cell lysate (10^6 cells sonicated 20 pulses, 5 sec, 18 V, 4°C; Misonix XL-1000 ultrasonicator) in phosphate buffer saline (PBS) containing 175 μgml^{-1} phenylmethylsulfonide fluoride (PMSF), 5μgml^{-1} lysosyme and 1 mini-complete protease inhibitor tablet. Beads were then washed and stored at -80 °C.

Mass spectrometry

Bead-coupled proteins were digested overnight at 37°C with sequencing grade trypsin (12.5 μgml^{-1}; Promega) in 20μl 25 mM NH_4HCO_3. Digests were analyzed using a LTQ Velos Orbitrap (Thermo Fisher Scientific) coupled to a nano-LC Ultimate 3000 RSLCnano system (Thermo Fisher Scientific). Peptides were analysed in the orbitrap in full ion scan mode at a resolution of 30000 (at m/z 400) and with a mass range of m/z 400-1800. MS/MS data were searched against the NCBInr *Homo sapiens* and the SwissProt *Chlamydia trachomatis* databases. False Discovery Rate (FDR) was calculated using the reversed database approach with a 1% filter for strict FDR and 5% for relaxed FDR.

The presence of IPAM was verified. The Mascott score was 2395.22 with 10 peptides read 2-20 times. A differential analysis was applied to identify targets, using GFP and additional Inc proteins as a reference, and a threshold of >30 was applied to the Mascott scores.

Co-immunoprecipitation

24 h post transfection, protein-G magnetic beads (Dynabeads, Invitrogen) were coupled with anti-CEP170 (Invitrogen) or anti-GFP (Invitrogen) antibodies prior to incubation (45 min, rotating, 30°C) with lysate from HeLa cells expressing GFP-

IPAM[90-268] or GFP. After washing with PBS, proteins were eluted using 75 mM Tris HCl pH 7.4, 0.5M EDTA, 0.05% SDS and mixed with the same volume of loading buffer [80 mM Tris HCl pH6.8, 20% (v/v) glycerol, 0.16% (w/v) SDS, 20% (v/v) β-mercaptoethanol, 3mg.ml^{-1} bromophenol blue].

Protein electrophoresis and Western blotting

Proteins were analysed by SDS-PAGE using 14% (v/v) acrylamide gels (Prosieve, Lonza). For gel staining, Coomassie blue R250 staining was performed. For Western blotting, proteins were transferred overnight at 4°C. Nitrocellulose membranes were incubated (1 h) in TBS, 0.05% (v/v) Tween 20, 5% (w/v) skimmed milk (TBST-milk) before an overnight incubation at 4°C with primary antibody diluted in the same buffer. Primary antibodies were anti-GFP (Clontech), anti-CEP170 (Invitrogen), anti-His (Invitrogen) or anti-γ-tubulin (Sigma-Aldrich). Membranes were washed with TBST, incubated (1 h, RT) with appropriate secondary antibodies coupled to horseradish peroxidase (HRP, Invitrogen) in TBST-milk and finally wash in TBST. Chemiluminescence-based immunodetection of HRP was performed according to the manufacturer's instructions (ECL, GE Healthcare). Films (GE Healthcare) were exposed, developed (Xograph) and scanned (Epson).

For densitometry, the protein of interest (CEP170) and a loading control (γ-tubulin) were detected from the same membrane. The 'gel analysis' algorithm in Fiji (Eliceiri et al., 2012) was used. A double ratio was used to simultaneously correct for loading and to compare to the control:

%reduction = $(\text{intensity}_{\text{CEP170}}/\text{intensity}_{\gamma\text{-tubulin}})_{\text{siRNA}}/(\text{intensity}_{\text{CEP170}}/\text{intensity}_{\gamma\text{-tubulin}})_{\text{control}}$

References:

Abdelrahman, Y.M. and Belland, R.J. (2005). The chlamydial developmental cycle. *FEMS Microbiol. Rev.* **29,** 949-59.

Al-Younes, H.M., Al-Zeer, M.A., Khalil, H., Gussmann, J., Karlas, A., Machuy, N., Brinkmann, V., Braun, P.R. and Meyer, T.F. (2011). Autophagy-independent function of MAP-LC3 during intracellular propagation of *Chlamydia trachomatis*. *Autophagy* **7,** 814-28.

Al-Zeer, M.A., Al-Younes, H.M., Kerr, M., Abu-Lubad, M., Gonzales, E. Brinkmann, V. and Meyer, T.F. (2014). *Chlamydia trachomatis* remodels stable microtubules to coordinate Golgi stack recruitment to the Chlamydial inclusion surface. *Mol. Microbiol.* **94,** 1285-97.

Alzhanov, D.T., Weeks, S.K., Burnett, J.R. and Rockey, D.D. (2009). Cytokinesis is blocked in mammalian cells transfected with *Chlamydia trachomatis* gene CT223. *BMC Microbiol*. **9,** 2-9.

Archuleta, T.L., Du, Y., English, C.A., Lory, S., Lesser, C., Ohi, M.D., Ohi, R. and Spiller, B.W. (2011). The *Chlamydia* effector chlamydial outer protein N (CopN) sequesters tubulin and prevents microtubule assembly. *J. Biol. Chem.* **286,** 33992-8.

D'Avino, P.P., Savoia, M.S. and Glover, D.M. (2005). Cleavage furrow formation and ingression during animal cytokinesis: a microtubule legacy. *J. Cell Sci.* **118,** 1549-58.

Bannantine, J.P., Griffiths, R.S., Viratyosin, W., Brown, W.J. and Rockey, D.D. (2000). A secondary structure motif predictive of protein localization to the chlamydial inclusion membrane. *Cell. Microbiol.* **2,** 35-47.

Beatty, W.L. (2006). Trafficking from CD63-positive late endocytic multivesicular bodies is essential for intracellular development of *Chlamydia trachomatis*. *J. Cell Sci.* **119,** 350-9.

Carabeo, R.A., Mead, D.J. and Hackstadt, T. (2003). Golgi-dependent transport of cholesterol to the *Chlamydia trachomatis* inclusion. *Proc. Natl. Acad. Sci. U.S.A.* **100,** 6771–6776.

Cocchiaro, J.L., Kumar, Y., Fischer, E.R., Hackstadt, T. and Valdivia, R.H. (2008). Cytoplasmic lipid droplets are translocated into the lumen of the *Chlamydia trachomatis* parasitophorous vacuole. *Proc. Natl. Acad. Sci. U.S.A.* **105,** 9379-84.

Delevoye, C., Nilges, M., Dehoux, P., Paumet, F., Perrinet, S., Dautry-Varsat, A. and Subtil, A. (2008). SNARE Protein Mimicry by an Intracellular Bacterium. *PLoS Pathog.* **4,** e1000022.

Dumoux, M., Clare, D.K., Saibil, H.R. and Hayward, R.D. (2012). *Chlamydiae* assemble a pathogen synapse to hijack the host endoplasmic reticulum. *Traffic* **13,** 1612-27.

Eliceiri, K.W., Berthold, M.R., Goldberg, I.G., Ibáñez, L., Manjunath, B.S., Martone, M.E., Murphy, R.F., Peng, H., Plant, A.L., Roysam, B. et al. (2012). Biological imaging software tools. *Nat. Methods* **9,** 697–710.

Gauliard, E., Ouellette, S., Rueden, K.J. and Ladant, D. (2015). Characterization of interactions between inclusion membrane proteins from *Chlamydia trachomatis*. *Front. Cell. Infect. Microbiol*. **5**, 13.

Grieshaber, S.S., Grieshaber, N.A., Miller, N. and Hackstadt, T. (2006). *Chlamydia trachomatis* causes centrosomal defects resulting in chromosomal segregation abnormalities. *Traffic* **7,** 940-9.

Guarguaglini, G., Duncan, P.I., Stierhof, Y.D., Holmström, T., Duensing, S. and Nigg, E.A. (2005). The forkhead-associated domain protein Cep170 interacts with Polo-like kinase 1 and serves as a marker for mature centrioles. *Mol. Biol. Cell* **16,** 1095-107.

Hoare, A., Timms, P., Bavoil, P.M. and Wilson, D.P. (2008). Spatial constraints within the chlamydial host cell inclusion predict interrupted development and persistence. *BMC Microbiol*. **8**, 5.

Hybiske, K. and Stephens, R.S. (2007). Mechanisms of host cell exit by the intracellular bacterium *Chlamydia. Proc. Natl. Acad. Sci. U.S.A.* **104,** 11430-5.

Jewett, T.J., Fischer, E.R., Mead, D.J. and Hackstadt, T. (2006). Chlamydial TARP is a bacterial nucleator of actin. *Proc. Natl. Acad. Sci. U.S.A.* **103,** 15599-604.

Johnson, K.A., Tan, M. and Sütterlin, C. (2009). Centrosome abnormalities during a *Chlamydia trachomatis* infection are caused by dysregulation of the normal duplication pathway. *Cell. Microbiol.* **11,** 1064-73.

Koskela, P., Anttila, T., Bjørge, T., Brunsvig, A., Dillner, J., Hakama, M., Jellum, E., Lenner, P., Luostarinen, T., Pukkala, E., et al. (2000). *Chlamydia trachomatis* infection as a risk factor for invasive cervical cancer. *Int. J. Cancer* **85**, 35-9.

Kumar, Y. and Valdivia, R.H. (2008). Actin and intermediate filaments stabilize the *Chlamydia trachomatis* vacuole by forming dynamic structural scaffolds. *Cell Host Microbe* **4,** 159-69.

Lane, B.J., Mutchler, C., Al Khodor, S., Grieshaber, S.S. and Carabeo, R.A. (2008). Chlamydial entry involves TARP binding of guanine nucleotide exchange factors. *PLoS Pathog.* **4,** e1000014.

Leonhardt, R.M., Lee, S.J., Kavathas, P.B. and Cresswell, P. (2007). Severe tryptophan starvation blocks onset of conventional persistence and reduces reactivation of *Chlamydia trachomatis*. *Infect. Immun.* **75,** 5105-17.

Lutter, E.I., Martens, C. and Hackstadt, T. (2012). Evolution and conservation of predicted inclusion membrane proteins in *Chlamydiae*. *Comp. Funct. Genomics* **2012,** 362104-18.

Maliga, Z., Junqueira, M., Toyoda, Y., Ettinger, A., Mora-Bermúdez, F., Klemm, R.W., Vasilj, A., Guhr, E., Ibarlucea-Benitez, I., Poser, I., et al. (2013). A genomic toolkit to investigate kinesin and myosin motor function in cells. *Nat. Cell Biol.* **15,** 325-34.

Miroux, M. and Walker, J.E. (1996). Over-production of proteins in *Escherichia coli*: mutant hosts that allow synthesis of some membrane proteins and globular proteins at high levels. *J. Mol. Biol.* **260,** 289-98.

Mital, J., Miller, N.J., Fisher, E.R. and Hackstadt, T. (2010). Specific chlamydial inclusion membrane proteins associate with active Src family kinases in microdomains that interact with the host microtubule network. *Cell. Microbiol.* **12,** 1235-49.

Mital, J., Lutter, E.I., Barger, A.C., Dooley, C.A. and Hackstadt, T. (2015). *Chlamydia trachomatis* inclusion membrane protein CT850 interacts with the dynein light chain DYNLT1 (Tctex1). *Biochem. Biophys. Res. Commun*. **462,** 165-70.

Nans, A., Saibil, H.R. and Hayward, R.D. (2014). Pathogen-host reorganization during *Chlamydia* invasion revealed by cryo-electron tomography. *Cell. Microbiol*. **16**, 1457-72

Nigg, E.A. (2002). Centrosome aberrations: cause or consequence of cancer progression? *Nat. Rev. Cancer* **2,** 815-25.

Peters, J., Wilson, D.P., Myers, G., Timms, P. and Bavoil, P.M. (2007). Type III secretion à la *Chlamydia*. *Trends Microbiol.* **15,** 241-51.

Radhakrishman, G.K. and Splitter, G.A. (2012). Modulation of host microtubule dynamics by pathogenic bacteria. *Biomol. Concepts* **3,** 571-580.

Richards, T.S., Knowlton. A.E. and Grieshaber, S.S. (2013). *Chlamydia trachomatis* homotypic inclusion fusion is promoted by host microtubule trafficking. *BMC Microbiol*. **13,** 185-96.

Romano, J.D., de Beaumont, C., Carrasco, J.A., Ehrenman, K., Bavoil, P.M. and Coppens, I. (2013). Fierce competition between *Toxoplasma* and *Chlamydia* for host cell structures in dually infected cells. *Eukaryotic Cell* **12,** 265-77.

Rzomp, K.A., Moorhead, A.R. and Scidmore, M.A. (2006). The GTPase Rab4 Interacts with *Chlamydia trachomatis* Inclusion Membrane Protein CT229. *Infect. Immun.* **74,** 5362–73.

Schmid, B., Schindelin, J., Cardona, A., Longair, M. and Heisenberg, M. (2010). A high-level 3D visualization API for Java and ImageJ. *BMC Bioinformatics* **11,** 274.

Schwan, C., Stecher, B., Tzivelekidis, T., van Ham, M., Rohde, M. Hardt, W.D., Wehland, J. and Aktories, K. (2009). *Clostridium difficile* toxin CDT induces formation of microtubule-based protrusions and increases adherence of bacteria. *PLoS Pathog.* **5,** e1000626.

Scidmore, M.A. and Hackstadt, T. (2001). Mammalian 14-3-3 beta associates with the *Chlamydia trachomatis* inclusion membrane via its interaction with IncG. *Mol. Microbiol.* **39,** 1638-50.

Smith, J.S., Bosetti, C., Muñoz, N., Herrero, R., Bosch, F.X., Eluf-Neto, J., Meijer, C.J., Van Den Brule, A.J., Franceschi, S., Peeling, R.W., et al. (2004). *Chlamydia trachomatis* and invasive cervical cancer: a pooled analysis of the IARC multicentric case-control study. *Int. J. Cancer* **111,** 431-9.

Welburn, J.P.I. and Cheeseman, I. (2012). The microtubule-binding protein Cep170 promotes the targeting of the kinesin-13 depolymerase Kif2b to the mitotic spindle. *Mol. Biol. Cell* **23,** 4786-4795.

Wilson, D.P., Timms, P., McElwain, D.L. and Bavoil, P.M. (2006). Type III secretion, contact-dependent model for the intracellular development of *Chlamydia*. *Bull. Math. Biol.* **68** , 161-78.

Woodruff, J.B., Wueseke, O. and Hyman, A.A. (2014). Pericentriolar material structure and dynamics. *Phil. Trans. R. Soc. B* **369,** 459-60.

Figures
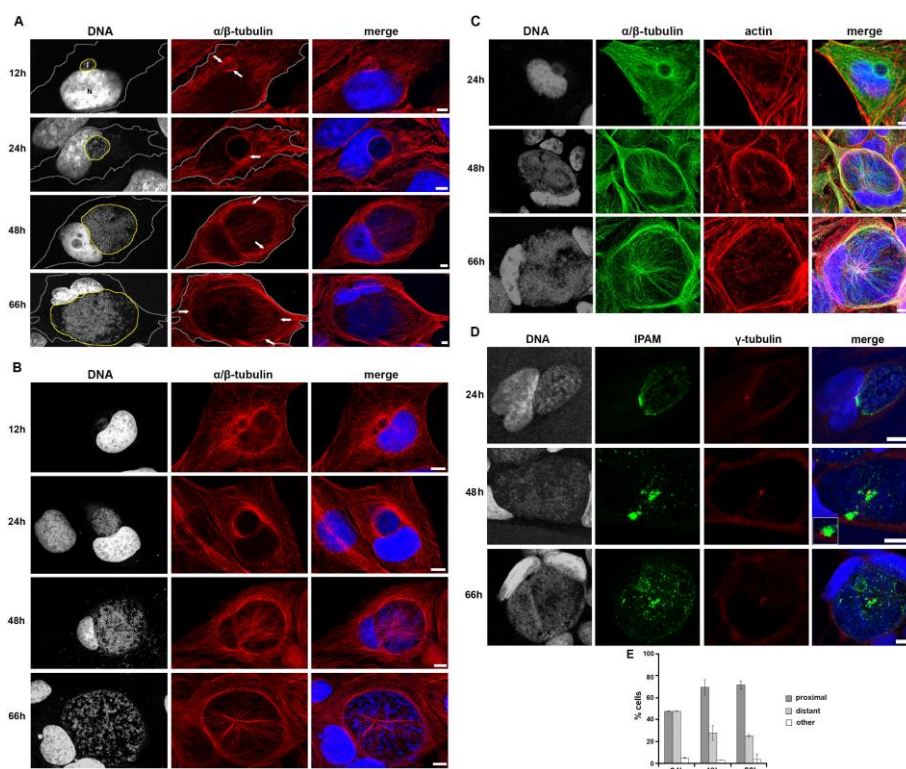
Fig 1: Cytoskeletal organization and γ-tubulin positioning in cells infected with _C.trachomatis._

HeLa cells (**A**) or U2OS cells (**B**) were infected with _C.trachomatis_ and incubated for 12, 24, 48 and 66 h, prior to fixation and staining for α/β-tubulin (red) or DNA (grey/blue). Panels show maximum projection of 4 z-slices. In **A** the cell periphery and the inclusion are outlined in grey and yellow, respectively. Arrows indicate the MT scaffold. Scale bar: 5 μm. (**C**) HeLa cells were infected with _C.trachomatis_ and fixed after 24 h, 48 h or 66 h. Cells were stained for DNA (grey/blue), α/β-tubulin (green) and actin (red). Panels show maximum projections obtained from the 4 z-sections shown. Scale bar: 10 μm. (**D**) HeLa cells were infected with _C.trachomatis_ and fixed after 24 h, 48 h or 66 h. Cells were stained for DNA (grey/blue), endogenous IPAM (green) and γ-tubulin (red). Patches of endogenous IPAM are visible at the inclusion membrane as described in **Fig S2A**. Asterisks indicate IPAM patches proximal γ-tubulin foci. Inset shows the indicated region in a different z-section. Panels show maximum projection of 4 z-sections. Scale bar: 10 μm. (**E**) Histogram shows quantification of the proximity of IPAM patches and the centrosome from confocal imaging (**Fig S2A**).

Fig 2: Impact of GFP-IPAM$^{90-268}$ on MT organization, centrosome integrity and MT assembly.

(**A**) HeLa cells expressing GFP-IPAM$^{90-268}$ (green) were fixed and stained for γ-tubulin or pericentrin (red). Fluorescence panels show maximum projection of 3 confocal z-sections spanning the centrosome. Scale bar: 5μm. (**B**) 3D reconstructions from structural illumination microscopy (SIM). Scale bar: 2 μm. (**C**) Representative images of HeLa cells expressing high levels of GFP-IPAM$^{90-268}$ (green) were fixed and stained

for γ-tubulin (red, upper) or pericentrin (red, lower). Scale bars: 5 μm. (**D**) Following confocal imaging, the features of the γ-tubulin (upper) or pericentrin (lower) labeling were categorized (as shown in **Fig S2B**) using cells expressing GFP, GFP-IPAM$^{90-268\ low}$ or GFP-IPAM$^{90-268\ high}$. *:p<0.05, **:p<0.01, ***:p<0.005. (**E**) HeLa cells expressing low or high levels of GFP-IPAM$^{90-268}$ (green) were fixed and stained for α/β-tubulin (red). Panels show maximum projection of the entire z-stack. Scale bar: 5 μm. (**F**) HeLa cells were transfected with GFP-IPAM$^{90-268}$ or GFP (green) and labeled for DNA (blue) and for α/β-tubulin (red). Panels show cells in division. Scale bar: 5 μm. (**G**) MTs were depolymerized in HeLa cells expressing GFP-IPAM$^{90-268}$ (green) and allowed to regrow for 5 min prior to fixation and staining for α/β-tubulin (red). Panels show maximum projection of 4 confocal z-sections. Cell periphery is outlined in white, and N indicates the nucleus. Scale bar: 5 μm. (**H**) MTs were depolymerized in HeLa cells expressing GFP, GFP-IPAM$^{90-268\ low}$ or GFP-IPAM$^{90-268\ high}$ (green). Panels show SIM reconstructions of MTs allowed to regrow for 5 min prior to fixation and staining for α/β-tubulin (red). The control GFP signal is absent as diffuse signals cannot be visualized by SIM. Scale bar: 2 μm. (**I**) Following confocal imaging, MT architecture in individual cells expressing GFP or GFP-IPAM$^{90-268}$ was categorized (as shown in **Fig S2C**) after MT depolymerisation and 5min regrowth. *** p<0.005.
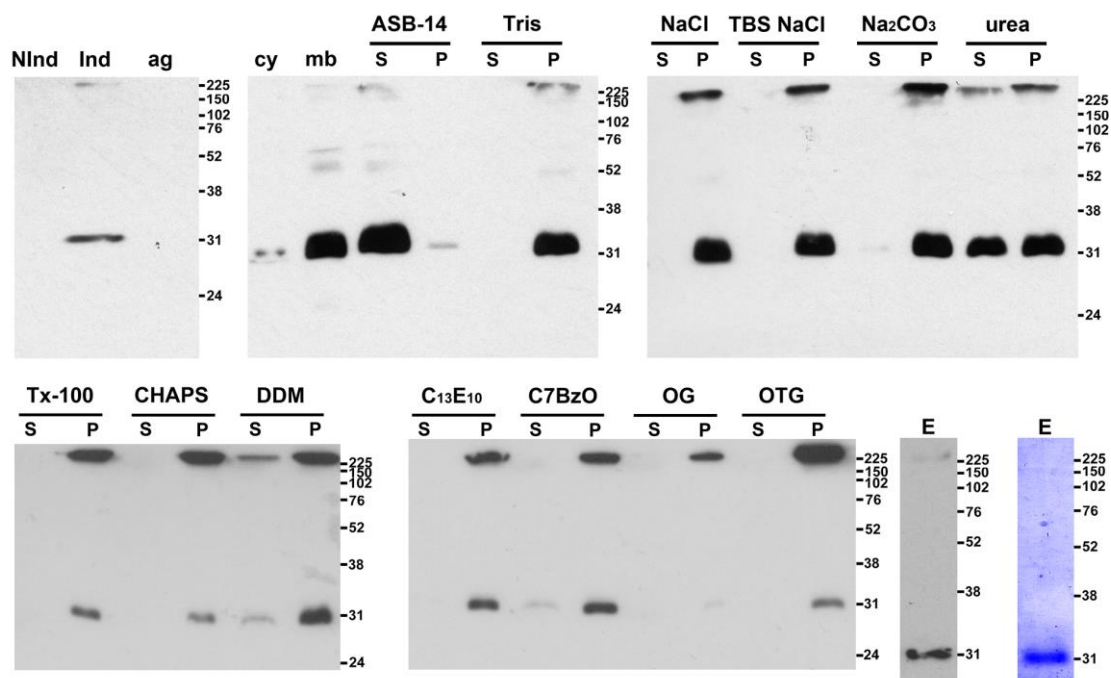
Fig 3: Native affinity purification of IPAM from *E.coli*.

Immunoblots with anti-His$_6$ antibody of SDS-PAGE separated fractions from *E.coli* transformants expressing IPAM. Cell lysates before (Nind) and after induction with IPTG (Ind) are shown together with pellet following low speed centrifugation to remove aggregated proteins and unlysed cells (agg), bacterial cytosol (cy) and membrane (mb) fractions. Membranes were incubated with buffers [20 mM Tris-Cl pH7.4 (Tris), 20 mM Tris-Cl pH7.4 140 mM NaCl (NaCl), 20 mM Tris-Cl pH7.4 1 M NaCl (Tris NaCl), 100 mM Na$_2$CO$_3$ pH11 (Na$_2$CO$_3$), 8 M urea (urea)] or detergents in TBS [1% ASB-14, Triton-X-100 (Tx-100), CHAPS, dodecylmaltoside (DDM), C$_{13}$E$_{10}$, C7BzO, OG and OTG] prior to centrifugation to separate solubilized proteins in the supernatant (S) from the membrane pellet (P). IPAM is present at the expected molecular weight (32kDa, arrow) and multimers IPAM are also evident (asterisk). Immunoblot and Coomassie-blue stained elution (E) are shown after affinity purification in 1% ASB-14. Molecular weight markers are shown in kDa (right).
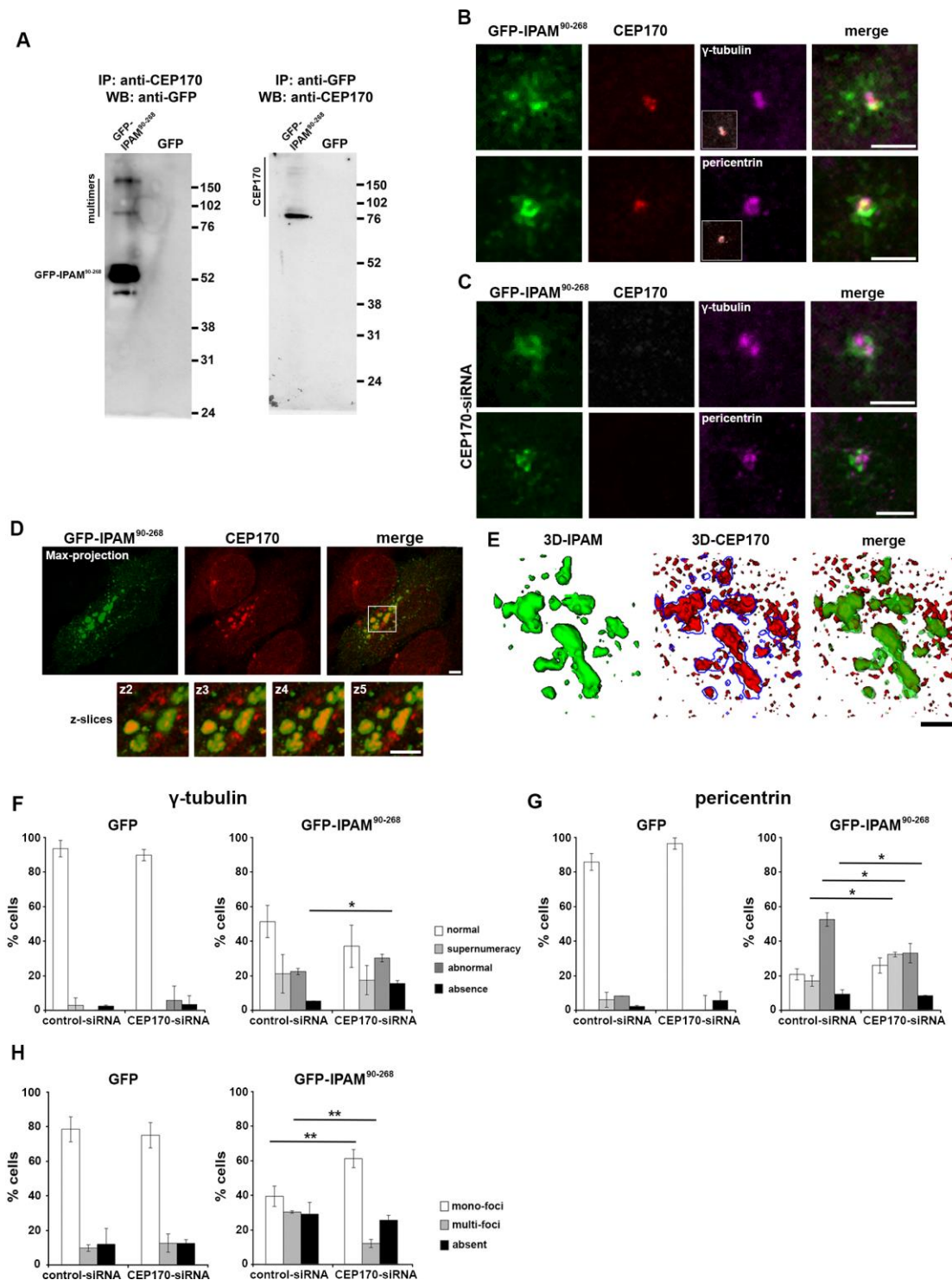
Fig 4: Functional interaction between GFP-IPAM$^{90\text{-}268}$ and CEP170.

(**A**) Immunoblots (WB) with anti-CEP170 or anti-GFP antibodies of SDS-PAGE-separated proteins immunoprecipitated (IP) with anti-CEP170 or anti-GFP. IPAM multimers are evident (see **Fig 3**). Positions of molecular weight markers (kDa) are indicated (right). (**B**) HeLa cells expressing low levels of GFP-IPAM$^{90\text{-}268}$ (green) were

fixed and co-stained for γ-tubulin or pericentrin (magenta/grey) and CEP170 (red). Insets show CEP170 (red) and γ-tubulin or pericentrin (grey) labeling only. Scale bar: 2 μm. (**C**) HeLa cells treated with CEP170-siRNA and expressing GFP-IPAM[90-268] (green) were fixed and co-stained for γ-tubulin or pericentrin (magenta) and CEP170 (red). Scale bar: 2 μm. (**D**) HeLa cells expressing high levels of GFP-IPAM[90-268] (green) were fixed and stained for CEP170 (red). Panels show maximum projections of 4 confocal z-sections (left). Scale bar: 5 μm. Insets show indicated region at higher magnification (right) broken down into individual z-sections (2-5). Scale bar: 2 μm. (**E**) 3D reconstructions from structural illumination microscopy, demonstrating that GFP-IPAM[90-268] co-localizes with CEP170. Scale bar: 2 μm. (**F**) γ-tubulin (left) or pericentrin (right) labeling was categorized (as described in **Fig S2B**) in HeLa cells treated with CEP170-siRNA or control-siRNA expressing GFP or GFP-IPAM[90-268] as indicated. *:$p<0.05$. (**G**) Quantification of the MT network (as described in **Fig S2C**) in HeLa cells treated with CEP170-siRNA or control-siRNA expressing GFP or GFP-IPAM[90-268] as indicated. **:$p<0.01$.
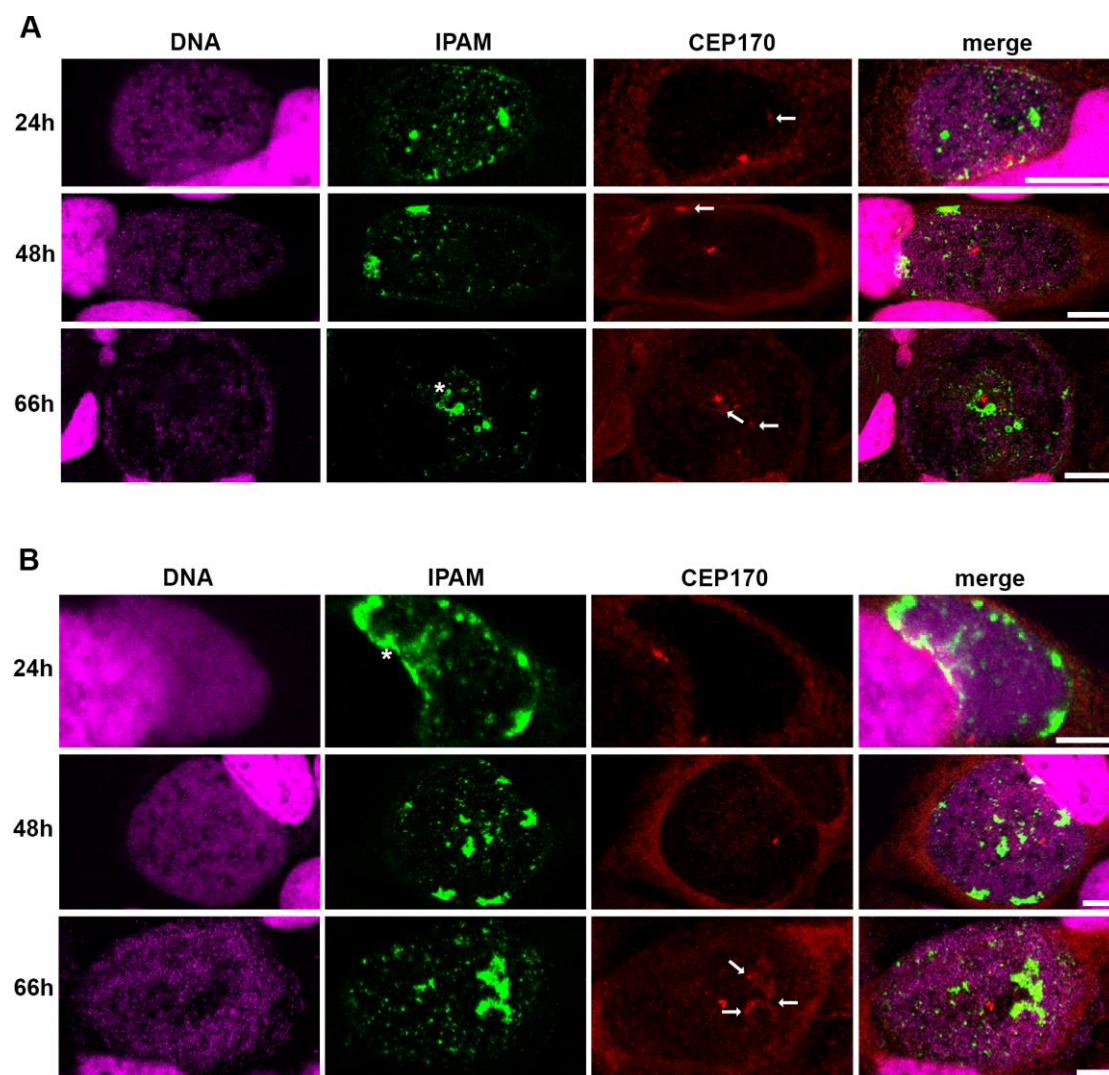
**Fig 5: IPAM and CEP170 location in *C.trachomatis* infected cells.**

HeLa cells (**A**) or U2OS cells (**B**) were infected with *C.trachomatis* for 24 h, 48 h or 66 h and labeled for DNA (grey/magenta), endogenous IPAM (green) and CEP170 (red). Asterisk indicates IPAM patches (as described in **Fig S2A**) in proximity of CEP170 dots. Arrows indicate diffuse CEP170 signal associated to IPAM. Scale bar: 10 µm.
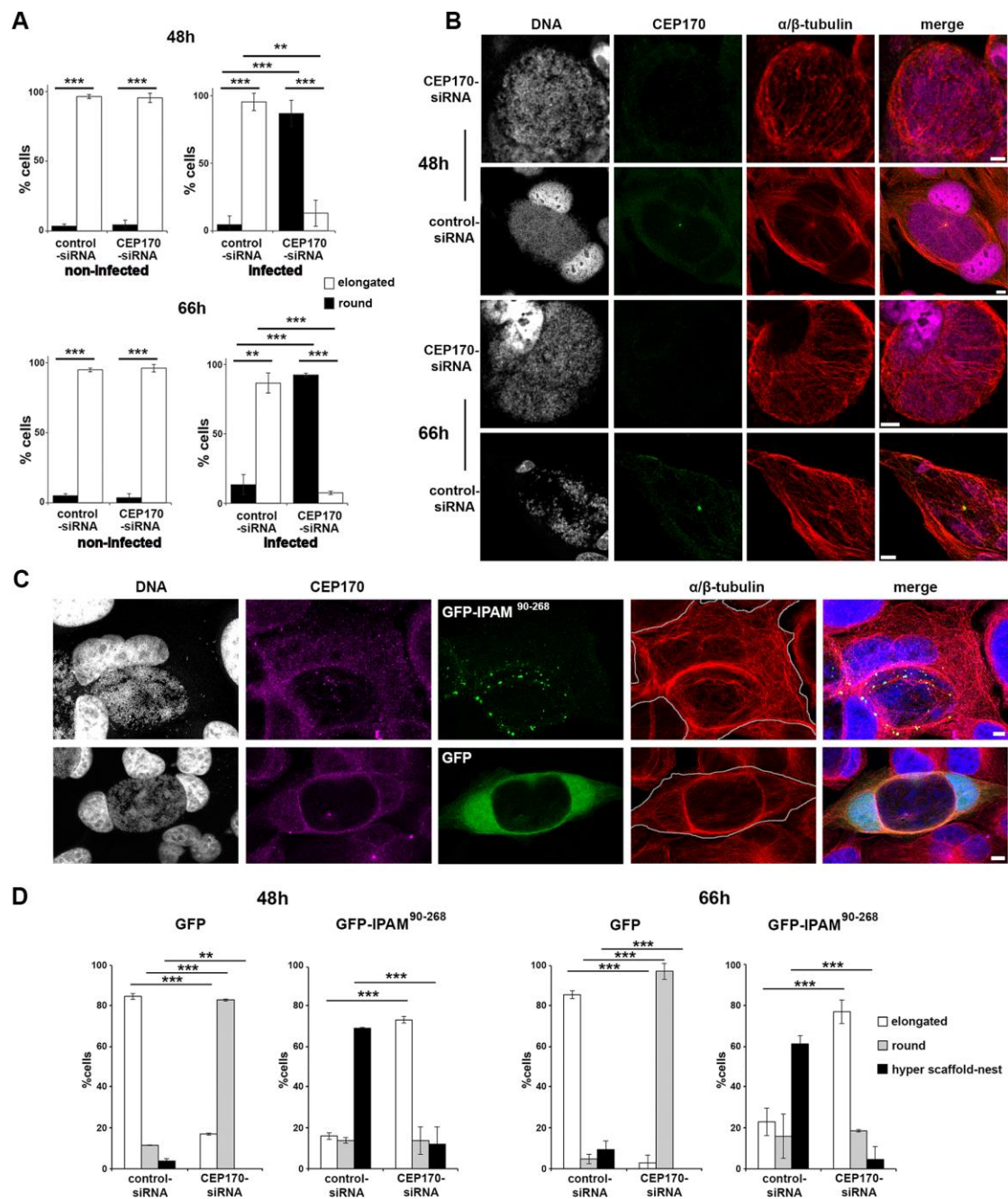
Fig 6: CEP170-IPAM interaction is essential to maintain cell shape and microtubule organization in *Chlamydia*-infected cells.

(**A**) HeLa cells were treated with control-siRNA or CEP170-siRNA, and infected with *C.trachomatis* where appropriate. Cell shape was assessed and categorized after 48 h or 66 h. Cells in mitosis identified by DNA staining were excluded. ****:p<0.01, ***:p<0.005. (**B**) HeLa cells treated with CEP170-siRNA or control-siRNA were infected with *C.trachomatis* and fixed after 48 h or 66 h. Cells were stained for DNA (grey), CEP170 (green) and α/β-tubulin (red). Panels show maximum projections of 4

z-sections. Scale bar: 10 μm. (**C**) HeLa cells were treated with CEP170-siRNA or control-siRNA for 24 h, prior to infection with *C.trachomatis* and transfection with plasmid encoding GFP or GFP-IPAM[90-268] (green). 48 or 66 h later cells were fixed and labeled for DNA (grey/blue) CEP170 (purple) and α/β-tubulin (red). Panels represent maximum projections of 4 z-sections in cells 48 h after infection, showing a representative 'hyper scaffold-nest'. The cell periphery is outlined in grey. Scale bar: 5 μm. (**D**) Following confocal imaging, cells shape was categorized (as described in **Fig S2E**) for *C.trachomatis* infected cells. ***:p<0.005, **:p<0.01.
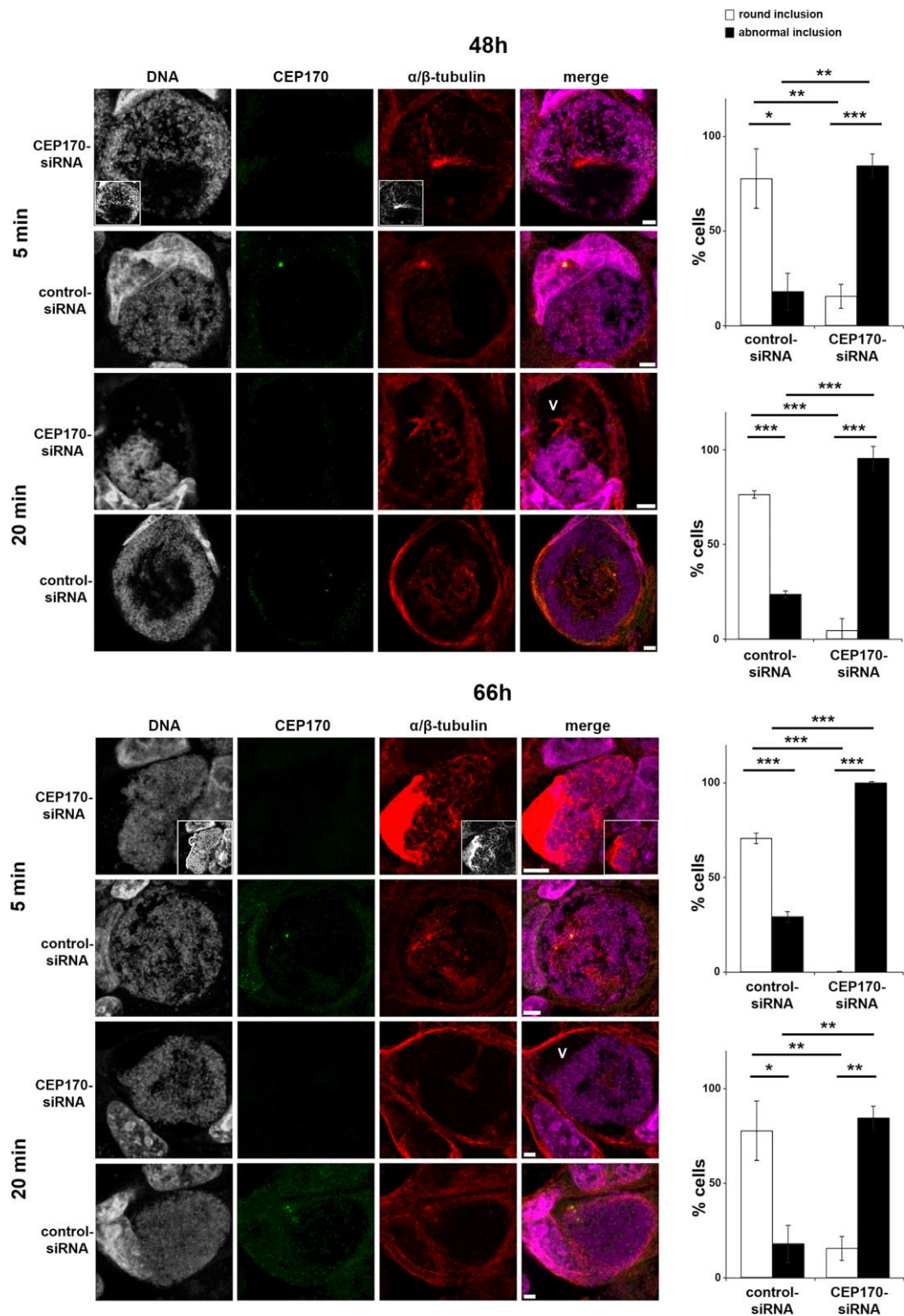
Fig 7: CEP170 knockdown impairs microtubule assembly in cells infected with *C.trachomatis.*

HeLa cells were treated with CEP170-siRNA or control-siRNA and infected with *C.trachomatis.* After 48 h (upper panels) or 66 h (lower panels), MTs were

depolymerized then allowed to regrow for 5 or 20 min prior to fixation. Cells were stained for DNA (grey/magenta), CEP170 (green) and α/β-tubulin (red). Panels show maximum projections of 4 z-sections. Void (V) is marked within an aberrant inclusion. Scale bars: 10 μm. Histograms show assessment of inclusion morphology (as described in **Fig S2F**) under the conditions indicated. ***:p<0.005, **:p<0.01,*:p<0.05.
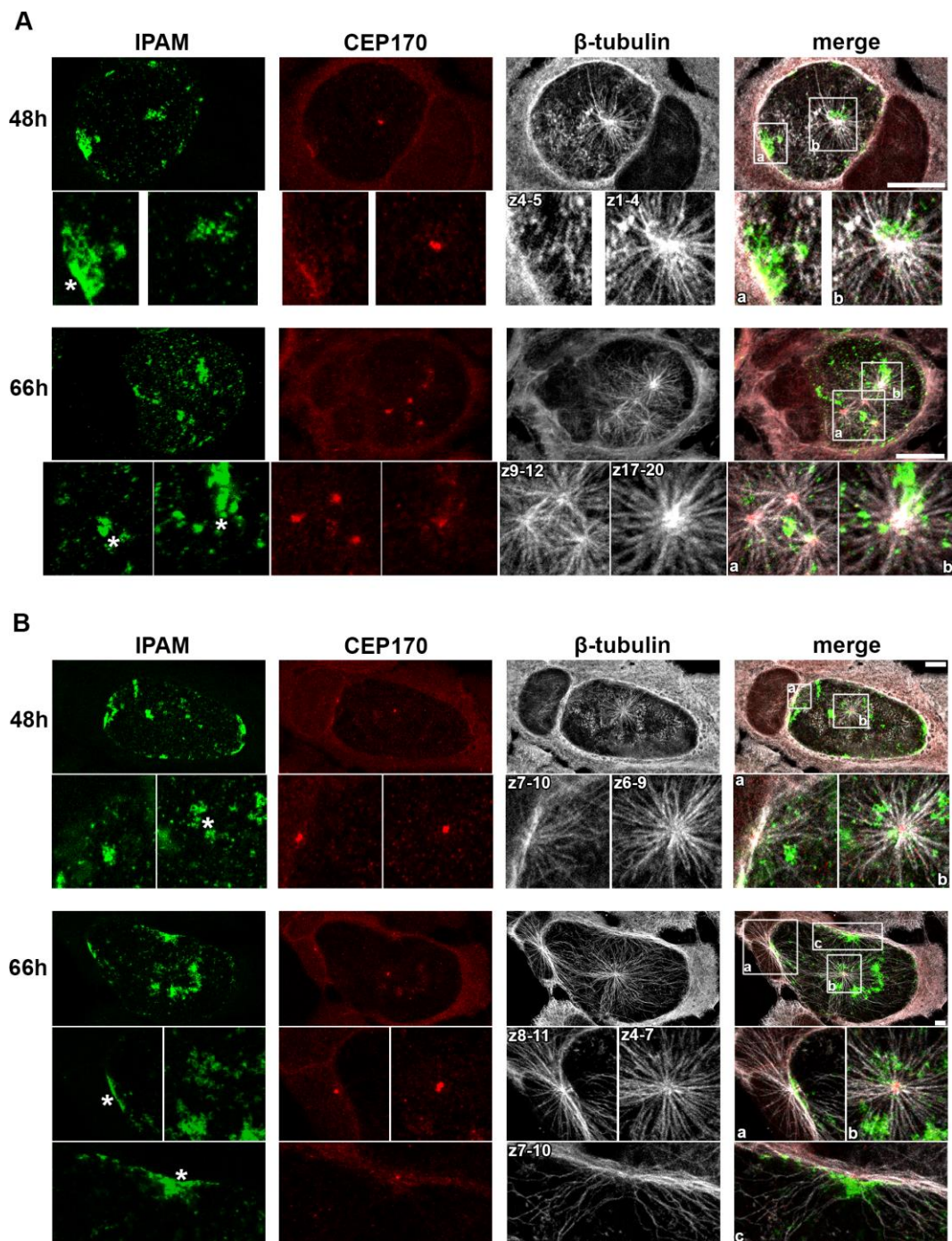
Fig 8: Endogenous IPAM localizes to sites of microtubule assembly in _C.trachomatis_ infected cells.

HeLa cells (**A**) or U2OS cells (**B**) were infected with _C.trachomatis_ for 48 h or 66 h prior to MT regrowth for 5 min. Cells were fixed and labeled for endogenous IPAM (green), CEP170 (red) and β-tubulin (grey). Upper panels show max-projections through the entire cell volume. Lower panels, show the max projection of the indicated z-section from the marked region of interest. Asterisks indicate the IPAM patches where MT regrow. Scale bar: 10 μm.